This is a preprint of a published paper, in "Composite Structures" by Elsevier availabe at https://doi.org/10.1016/j.compstruct.2018.01.075

# An insight into the low-velocity impact behavior of patch-repaired CFRP laminates using numerical and experimental approaches

Ying Tie[a], Yuliang Hou[a,b,*], Cheng Li[a], Xihui Zhou[a], Thaneshan Sapanathan[b,c], Mohamed Rachik[b]

[a] *School of Mechanical Engineering, Zhengzhou University, Science Road 100, 450001, Zhengzhou,China*
[b] *Laboratoire Roberval, CNRS UMR7337, Sorbonne université, Université de Technologie de Compiègne, Centre de recherche Royallieu, CS60319, 60203, Compiègne Cedex, France*
[c] *Institute of Mechanics, Materials and Civil Engineering, Université catholique de Louvain, B-1348 Louvain-la-Neuve, Belgium*

## Abstract

In this paper, the low-velocity impact response of patch-repaired CFRP laminates is investigated experimentally and numerically. This study considers various patches of different shapes and sizes placed on the single side of the parent laminate plates. In the low-velocity impact simulation, damage development and the failure process of the repaired laminate plates are analyzed based on continuum damage mechanics (CDM) theory which is derived from 3D Hashin failure criteria, and a cohesive zone model (CZM). In order to validate the proposed numerical approach, impact response such as impact force and energy are predicted from simulation. Moreover, the corresponding drop weight impact tests have been performed, and the numerical prediction is in a good agreement with the experimental measurements. Finally, the influence of patch parameters on repair performance has been analyzed according to the delamination surface area and absorbed energy of the repaired laminates from the low-velocity impact simulation. And, an optimal impact-resistance design of the patch repair is obtained based on the finding results.

*Keywords:* Composite structures, Impact behavior, Low-velocity impact, CFRP laminates, Patch-repair technique

## 1. Introduction

Due to the inherently excellent mechanical properties as well as low weight, composite materials such as carbon fiber reinforced polymer (CFRP) laminates, have become attractive alternatives for modern engineering applications, particularly in the transport industry (aeronautic, automotive and marine) [1]. Commonly, partial damage on CFRP laminates, which is caused by low-velocity impacts, leads to the reduction in local mechanical properties of the composite structures. And, it gives rise to the demand of repair rather than replacement as the first-time solution to reduce the

*Corresponding author.
*Email address:* yulianghou@zzu.edu.cn (Yuliang Hou)

maintenance cost [2]. Hence, the development of local patch repair technique makes it to meet the requirement of this engineering problem mechanically and economically.

In general, bonding composite patches to the locally damaged areas is a repairing technique which is widely used in the industry. From former research studies [3–8], it is found that, the repairing effect depends not only on the bonding process, but also on the patch design. Therefore, when the patch including its shape and size has been well-designed, it can reconstruct the mechanical performance of repaired composite structures, and perform like the original ones. However, the impact behavior of the repaired structures have been changed, and the integrity and stability of such structures decrease after the repairing process.

Whittingham et al. [9] have studied a scarf bonding method, in which a considerable quantity of parent material around the damage area needs to be removed from one side to give a depression with a quite low scarf angle and a hole in the middle. The depression is then filled by fitting and adjusting the required number of individual plies of prepreg material and consolidated by hot pressing under pressure. Although the results are satisfactory, the method requires special equipment and is time-consuming [10–12]. There is another repair technique, known as external bonded patch-repair technique, that is more convenient to apply than this one, but cannot reach the same efficiency [5, 13–17]. This technique leads to substantial stress concentration at the patch edges. Therefore, it requires more attention to the patch geometry, size, bond thickness and bond stiffness. Each parameter has its own influence on the final repair performance, and optimal repair controlling parameters can be obtained using a target function with these inputs. In the work of Soutis et al. [18], the compressive behavior of patched CFRP laminates has been investigated. And it concluded that repair performance depends heavily on the coherence between patch and parent material and the adhesive type. Liu et al. [14] repaired $[(0/90/45-45/90/0)_2]s$ laminates using external bonded patches and studied the tensile behavior of repairs as a function of patch lay-up and patch size. They found that, the failure of the repairs is mainly caused by the debonding of patches. Cheng et al. [16, 17] investigated the tensile behavior of patch-repaired CFRP laminates experimentally and numerically, and proposed related optimization of bonded patch repairs accordingly.

Additionally, these repaired composite structures are still susceptible to other low-velocity impact [19] of foreign objects during their remaining lifetime operation. Due to the reduction of impact resistance and weak interfaces of composite laminates, the impact damage often appears around the patch bonding location. For composite laminates, there are four principle failure modes: matrix cracking, fiber breakages, delamination and debonding [20, 21]. The matrix cracking and delamination are the most common damage occurred after low-velocity impact. Andrew et al. [22] repaired glass/epoxy laminates by removing the damage area with a circular cutout and filled with chopped fibers and patches. In their work, the impact response of both repaired and unpaired laminates has been investigated after repeated impact loading. And, the results showed that the repaired laminates had more enhanced capacity to resist a large number of impacts. Coelho et al. [23] studied the impact fatigue behavior of composite laminates repaired using various external bonded patches with different geometries experimentally. The best performance is obtained for the double-patch geometry, due to the higher stiffness.

In this paper, the primary CFPR composite laminate used is T300/7901. Damaged specimens are obtained using water-jet machine to cut circle holes, which are considered as the damage source. Various single patches with different shapes are adopted to repair these damaged specimens. Repaired specimens are subjected to low-velocity weight drop tests [20, 24]. Impact force curve and delamination surface area are measured for each specimen. Moreover, corresponding numerical simulations of low-velocity tests have been implemented to predict the impact behavior of repaired specimens. In these numerical works, a continuum damage mechanics (CDM) method based on 3D Hashin criteria [25–27] and a cohesive zone model (CZM) [28–30] are utilised to simulate the damage development and the delamination process of the repaired laminates. Comparison between experimental measurements and simulation results has also been carried out to validate the reliability of the proposed numerical simulation approach. Further investigation is performed to study the influence of patch geometry (including patch shape and size) on the repair performance.

The remainder of the paper is organized in the following manner: Section 2 briefly describes the experimental work; Section 3 presents the finite element (FE) modeling and the used material constitutive models; Section 4 initially validates the numerical analysis method, and introduces the repairing effect of various patch design parameters, finally proposes the optimal design; the paper ends with conclusions and perspectives.

## 2. Experimental work

### *2.1. Materials and specimen*

In this work, carbon fiber/epoxy composite laminates of stacking sequence $[(0/90)_3]_S$ with dimension of 150 mm × 100 mm × 3.6 mm were utilized as the parent plates. The composite laminate is composed of T300 carbon fiber and 7901 resin. Circular holes with the radius of $r$ = 3 mm were cut on these parent plates using water jet cutting machine, which were treated as the accidentally caused damage. Geometry information of the parent plates is given in Fig. 1(a).

Table 1: Mechanical properties of materials.

| Material | T300/7901 | Adhesive |
|---|---|---|
| $E_1(GPa)$ | 125 | 0.21 |
| $E_2, E_3(GPa)$ | 11.30 | |
| $\nu_{12}$ | 0.30 | |
| $\nu_{23}$ | 0.42 | |
| $\nu_{13}$ | 0.30 | |
| $G_{12}, G_{13}(GPa)$ | 5.43 | |
| $G_{23}(GPa)$ | 3.98 | |
| $X_t(MPa)$ | 2000 | |
| $X_c(MPa)$ | 1100 | |
| $Y_t, Z_t(MPa)$ | 80 | |
| $Y_c, Z_c(MPa)$ | 280 | |
| $S(MPa)$ | 120 | |
| $G^t_{IC}(N/mm)$ | 0.52 | |
| $G^c_{IC}(N/mm)$ | 0.92 | |

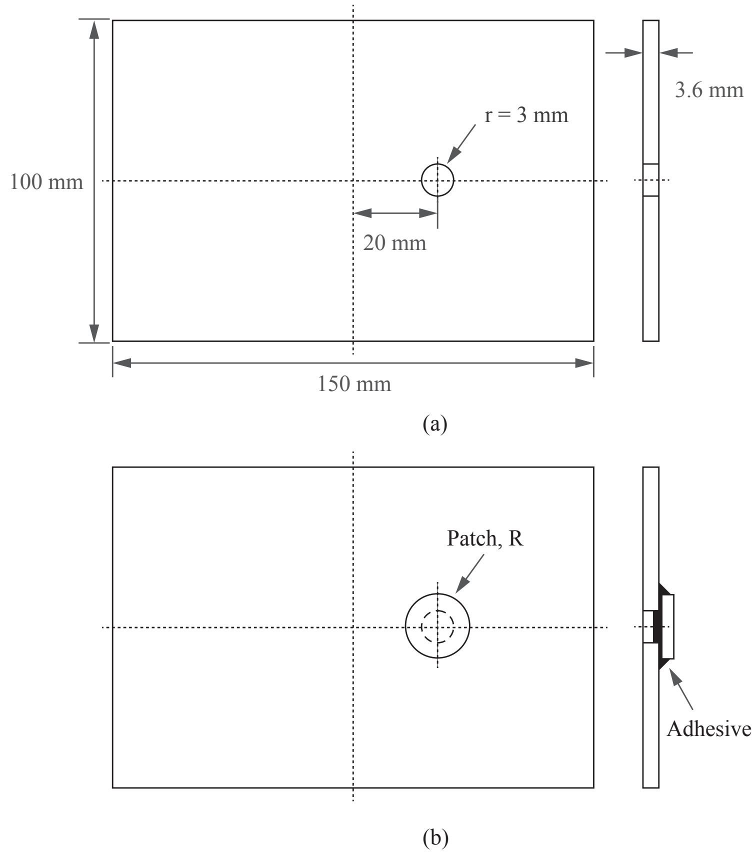


Figure 1: Geometry information of: (a) notched and (b) repaired plates.

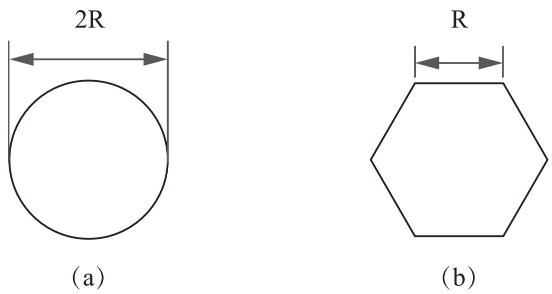


Figure 2: Geometry information of the patches with different shapes: (a) circle and (b) hexagon.

The damaged laminates are repaired using a single external patch design. Patches were manufactured from the same CFRP lamintes but with different stacking sequence [0/90/0], and their thickness is 0.45 mm. Totally, patches were prepared with two different shapes: (i) circle and (ii) hexagon, as shown in Fig. 2, since the numerical simulation (see Section 4.2.1) performed before the experimental work indicated that the circular and hexagonal patches provide better performance than others. Thus, experimental work was performed with these two beneficial patches to identify the most suitable patch geometry. Hence, these two patch shapes were selected in our test plan.

In the current test plan, the patches with cirle shape were manufactured with radius of $2r$. The hexagon patches were prepared with size, $R = 3.30$ mm, which makes the patch surface equal to the circle one. A toughened single part epoxy adhesive with a controlled 0.15 mm thick bond line was utilized to repair the damaged parent plates with different patches. The configuration of repaired specimens is illustrated in Fig. 1b. Mechanical properties of the used materials are given in Table. 1, where $E$ and $G$ refer to the Young's and shear modulus, and $\nu$ is the Poisson's ratio. Subscripts 1, 2, 3 correpond to the longitudinal and the two transverse directions, respectively. $X$, $Y$ and $S$ are logitudinal, transvers and shear strength, subscripts $t$ and $c$ denote tensile and compression.

### 2.2. Drop-weight test

A drop-weight impact test was designed according to the ASTM D7136/D7136-07 test standard [31], in which the repaired specimens were placed over a flat support with a 125 mm × 75 mm rectangular cut-out, as shown in Fig. 3a. This cut-out allows the impactor to contact through the specimen without interferences. Additionally, on the support fixture, four rubber clamps ware used to restrain the test specimen during the impact process. The damage hole was located 20 mm away from the center of the parent laminate and the center is considered as the impact point in the low-velocity impact test (Fig. 3a). Generally, when the damage location is at the center of the repaired specimen, due to the large impact energy, the adhesive bondline between the external patch and the parent laminate was severely damaged, which has been observed during experimental process. This phenomenon causes energy dissipation during the impact process, and makes it difficult to analyze the impact-resistance properties of parent laminate provided by the repairing patch.Thus, in order to minimize this complexity and to give particular attention to identify the impact-resistance properties of the repaired patches, the aforementioned damage hole locations were chosen in this study.

The hemispherical impactor, whose weight is 2.5 kg and radius is 25 mm, is placed at the initial height of 0.54 m to perform low-velocity impact tests (see Fig. 3b). And, an anti-impact device was utilized over the fixture to avoid secondary impact on the repaired specimen. During the impactor dropping process, it assumes that there is no energy loss due to friction, so that the impact velocity and energy are computed as 3.25 m/s and 13.2 J, respectively.

Experiments were carried out using WLJ 300 drop-weight impact test machine at room temperature. In these tests, the instantaneous impact force was measured by the dynamic force sensor (ICP 208C03). Initially, the acceleration of the impactor was recorded using the sensor. The impact force was computed automatically by multiplying the instantaneous acceleration with the mass of the impactor. For each specimen, a maximum force was reached before the impactor penetrated through the specimen. The onset of impact is defined by the sudden increase of impact force in the force-time curves.Additionally, the impact energy history curves were obtained by:

$$E(T) = \frac{1}{2} m \cdot (\int_0^T a(t)dt)^2 \tag{1}$$

where $m$ and $a(t)$ are the mass and the instantaneous acceleration of the impactor. Three repaired specimens for each patch geometry were tested to ensure the reproducibility of the results. The

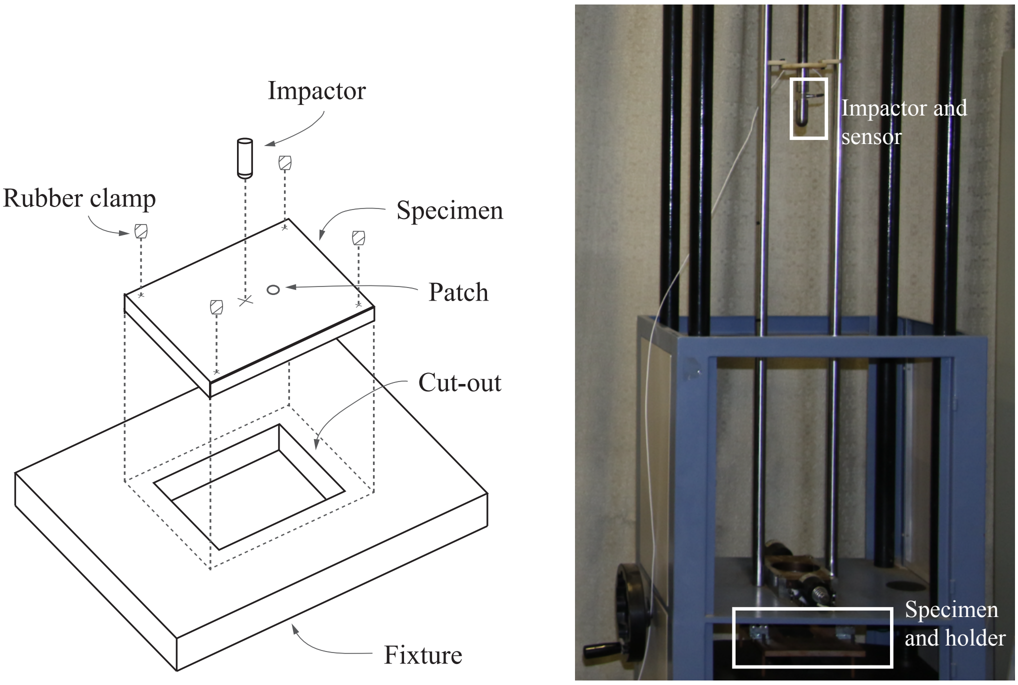


(a) (b)

Figure 3: (a) Schematic illustration of the drop-weight impact testing system and (b) the apparatus used in the experiments.

variations in these measured curves are around 1.5 % for each group of repaired specimens. Furthermore, in order to analyze the repair effect of each patch design, a group of unrepaired specimens were tested. The delamination surface area of each repaired specimen was then measured and considered as the parameter to evaluate the repair performance of different patch design.

## 3. Numerical simulation methodology

As presented in Section 2.2, the force-time curves and delamination area were obtained from the drop-weight tests of damaged and repaired laminates. However, in the aforementioned test plan, only circular and hexagonal patch designs are taken into consideration. Therefore, in order to analyze the repair effect and to determine the optimal patch design, this section is not only constructed with the numerical models for these tested specimen, but also extended to specimens with other patch designs, e.g., square and octagon. Moreover, details of the used material constitutive models, including a continuum damage model with 3D Hashin criteria and cohesive zone model, will be described.

### *3.1. Finite element modeling*

3D FE models of unrepaired and repaired specimens are constructed using Abaqus/Explicit [32] software. All specimens and related components of the test (including impactor, rapper clamps and fixture) are meshed with eight-node 3D solid, reduced integration elements (C3D8R in Abaqus/Explicit). Fig. 4 shows the details of the meshed FE model, including a repaired circular patch of $R = 2.5r$. A group of cohesive elements (type: COH3D8) are used to simulate the interface between the parent laminate and patch. In order to ensure the accuracy of the FE simulation, the parent laminate and patch are respectively discretized with 65239 and 53518 elements, since they have been proved to be fine enough to describe the damage behavior caused by impact [6].

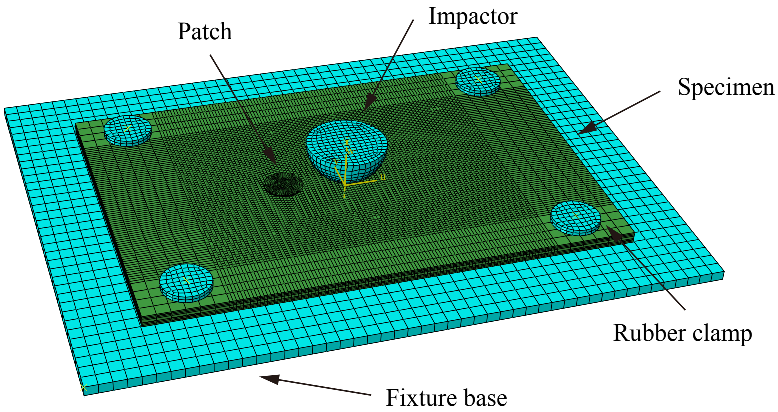


Figure 4: Illustration of the FE model of drop-weight impact test that includes the repaired specimen with a circular patch.

Boundary conditions are simulated by fixing all DOEs (degree of freedom) of the fixture base and rubber clamps. And, an initial velocity of 3.25 m/s in the vertical direction is prescribed to the impactor. In this paper, the drop weight tests of specimens repaired with circle and hexagon patches have been performed to validate the used simulation process. Moreover, specimens repaired with other patch shapes and sizes have also been constructed using this numerical approach to determine the optimal patch design parameters.

### *3.2. Constitutive models*

#### *3.2.1. Continuum damage model*

The residual strength of damaged laminate is described based on a continuum damage model (CDM), in which the influence of microscopic damage on macroscopic mechanical properties is quantified by the use of a state variable. Therefore, a damage variable $D_f$ is defined, its value increases with the growth in microscopic damage. After damage, the constitutive equation of material can be expressed as shown in Eq. (2):

$$\boldsymbol{\sigma} = \frac{\partial W^e}{\partial \boldsymbol{\varepsilon}} = (1 - D_f)\boldsymbol{C} : \boldsymbol{\varepsilon} \tag{2}$$

where, $\boldsymbol{\sigma}$ and $\boldsymbol{\varepsilon}$ present stress and strain tensor, $\boldsymbol{C}$ is the 4th order constitutive tensor. The range of the damage variable, $D_f$, is from 0 to 1, which corresponds to the primitive and damaged material states. $D_f$ is computed based on 3D Hashin failure criteria and the stress state in each element.

Based on the CDM theory, the loading capability of damaged elements, whose strength reduced with micro-cracks initiation, are distributed within those undamaged elements. In addition, for applying the same displacement, the residual strength of the damaged elements is given as:

$$E_i^D = (1 - D_f)E_i, \qquad G_{ij}^D = (1 - D_f)E_{ij}, \qquad \nu_{ij}^D = (1 - D_f)\nu_{ij} \tag{3}$$

where $E_i^D$, $G_{ij}^D$ and $\nu_{ij}^D$ are the effective Young's modulus, shear modulus and Poisson's ratio of material after damage, respectively. Correspondingly, $E_i$, $G_{ij}$ and $\nu_{ij}$ are Young's modulus, shear modulus and Poisson's ratio of material at the primitive status.

### *3.2.2. 3D Hashin progressive failure criteria*

In order to determine the intralaminar damage initiation and the final failure of composite laminates repaired with different patches, 3D Hashin failure criteria has been adopted in our numerical simulation. The main reason to select the Hashin failure criteria is that, it has been successfully used in numerous FE simulations to predict the progressive failure behavior of composite materials. Moreover, this failure criteria includes four individual failure modes: fiber and matrix failure, and includes both tensile and compressive mode [33]. In this criteria, material failure caused by delamination is not been considered. And, each failure mode is governed by the component of the stress tensor associated with the failure plane by a quadratic equation.

Fiber tensile failure mode ($\sigma_{11} \geq 0$):

$$(\frac{\sigma_{11}}{X_T})^2 + \frac{\sigma_{12}^2 + \sigma_{13}^2}{S^2} \geq 1 \tag{4}$$

Fiber compressive failure mode ($\sigma_{11} \leq 0$):

$$(\frac{\sigma_{11}}{X_C})^2 \geq 1 \tag{5}$$

Matrix tensile failure mode ($\sigma_{22} + \sigma_{33} \geq 0$):

$$\frac{(\sigma_{22} + \sigma_{33})^2}{Y_T^2} + \frac{\sigma_{12}^2 + \sigma_{13}^2 + \sigma_{23}^2 - \sigma_{22}\sigma_{33}}{S^2} \geq 1 \tag{6}$$

Matrix compressive failure mode ($\sigma_{22} + \sigma_{33} \leq 0$):

$$[(\frac{Y_C}{2S})^2 - 1]\frac{(\sigma_{22} + \sigma_{33})}{Y_C} + \frac{\sigma_{12}^2 + \sigma_{13}^2 + \sigma_{23}^2}{S^2} + \frac{\sigma_{22}^2 + \sigma_{33}^2}{2S^2} \geq 1 \tag{7}$$

where $\sigma_{ij}$ is component of stress tensor, and other material parameters are listed in Table 1. During the deformation process, once damage in the composite laminates or patches has been identified using the failure criteria of Eqs. (3-6), the stiffness matrix $\boldsymbol{C}$ in Eq. (2) corresponding to the FE equilibrium strain state to the stress must be updated at that particular analysis time step. The constitutive relation of the composite material is degraded by the material property degradation model (MDM) by following the detection of failed element in any of the four possible failure modes. In this paper, to simulate the strain-softening behavior of composite laminates, the CDM effective stress method is utilized with the continuous degradation damage variable $D_f$ [34], which is expressed as:

$$D_f = 1 - (1 - d_{ft})(1 - d_{fc}) \tag{8}$$

where

$$d_{ft}(\varepsilon_{11}) = \frac{\varepsilon^t_{f,1}}{\varepsilon^t_{f,1} - \varepsilon^t_{0,1}}(1 - \frac{\varepsilon^t_{0,1}}{\varepsilon_{11}}) \tag{9}$$

$$d_{fc}(\varepsilon_{11}) = \frac{\varepsilon^c_{f,1}}{\varepsilon^c_{f,1} - \varepsilon^c_{0,1}}(1 - \frac{\varepsilon^c_{0,1}}{\varepsilon_{11}}) \tag{10}$$

The superscripts $t$ and $c$ refer to tension and compression, respectively. $\varepsilon^t_{0,1}$ and $\varepsilon^c_{0,1}$ correspond to the tensile and compressive strains when the failure initially appears, $\varepsilon^t_{f,1}$ and $\varepsilon^c_{f,1}$ are the maximum strains in tension and compression at the final failure. The maximum failure strains $\varepsilon^t_{f,1}$ and $\varepsilon^c_{f,1}$ are computed by:

$$\varepsilon^t_{f,1} = \frac{2G^t_{IC}}{X_T L} \tag{11}$$

$$\varepsilon^c_{f,1} = \frac{2G^c_{IC}}{X_C L} \tag{12}$$

where $X_T$ and $X_C$ are respectively the tensile and compressive strengths in fiber direction, $G^t_{IC}$ and $G^c_{IC}$ are the intralaminar damage toughness in fiber under tension and compression (given in Table 1), $L$ is the characteristic length of an element.

To predict the failure of the composite material, 3D Hashin criteria has been implemented in Abaqus/Explicit [32] in the term of a user subroutine VUMAT, which includes the failure criteria, stiffness degradation of damaged elements and an element deletion criterion. At each loading step, the stresses at each integration point in the composite laminate are calculated in this user subroutine. Then, the failure criteria are used to evaluate whether any failure occurs or not, and the elastic properties at that particular element must be degraded according to the failure mode. A degradation procedure has also been introduced into the user subroutine to reproduce the damage to the material. Moreover, when a finite element is identified to be damaged based on the failure criteria, its stiffness is reduced, and large deformation appears. After progressive damage calculation, the final failure elements do not contribute to the strength of the composite laminate, but they produce the convergence in the simulation process.

#### *3.2.3. Cohesive zone model*

In this paper, the failure behavior of the adhesive bondline between damaged laminate and patch is described using a cohesive zone model (CZM) [35]. The interface area of two adjacent layers in the parent laminates can be regarded as a cohesive zone, which is also represented using the CZM model. That is, the CZM model is also used to simulate the inter-laminar damage of the composite laminate. Therefore, the delamination between layers of the parent laminate is predicted using the same cohesive elements. Moreover, the delamination area after impact is compared with the experimental measurements to validate the adopted simulation strategy. The CZM follows a traction-separation law in which the traction stress and separation displacement of the nodes on the surfaces are used in the calculation. This model is applied to predict damage onset and growth along the adhesive interface. The traction stress on a surface consists of 3 components: a normal and two shear tractions. The elastic behavior can be written as in Eq. (13):

$$\boldsymbol{t} = \begin{bmatrix} t_n \\ t_s \\ t_t \end{bmatrix} = \begin{bmatrix} C_n & 0 & 0 \\ 0 & C_s & 0 \\ 0 & 0 & C_t \end{bmatrix} \begin{bmatrix} \delta_n \\ \delta_s \\ \delta_t \end{bmatrix} \tag{13}$$

where, $\boldsymbol{t}$ is the traction stress vector, $\boldsymbol{\delta}$ is the separation displacement vector. And, the subscripts of interaction stiffness $C$ represent three directions that correspond to the three fracture modes.

In addition, the debonding damage between laminate and patch is controlled using a quadratic separation law. In this law, debonding appears when the quadratic interaction function reaches 1, which is given by:

$$(\frac{\langle \delta_n \rangle}{\delta_n^0})^2 + (\frac{\delta_s}{\delta_s^0})^2 + (\frac{\delta_t}{\delta_t^0})^2 \geq 1 \tag{14}$$

where, $\delta_n^0$, $\delta_s^0$ and $\delta_t^0$ denote the peak values of the contact separation, when the separation is either purely along the contact normal or purely in the first or the second shear direction, respectively. To ensure the prediction of the damage evolution under a combination of normal and shear separations across the cohesive interface, an effective separation $\delta_m$ is introduced by Eq. (15).

$$\delta_m = \sqrt{\langle \delta_n \rangle^2 + \delta_s^2 + \delta_t^2} \tag{15}$$

Similarly, the stress-strain relationship of these cohesive elements can be divided into two steps, as shown in Fig. 5. The mechanical behavior of the interaction between laminate and patch is considered to be linear elastic before appearance of the interface debonding (Step 1 in Fig. 5). Once the damage criteria is satisfied, the cohesive stiffness degrades linearly (Step 2 in Fig. 5).

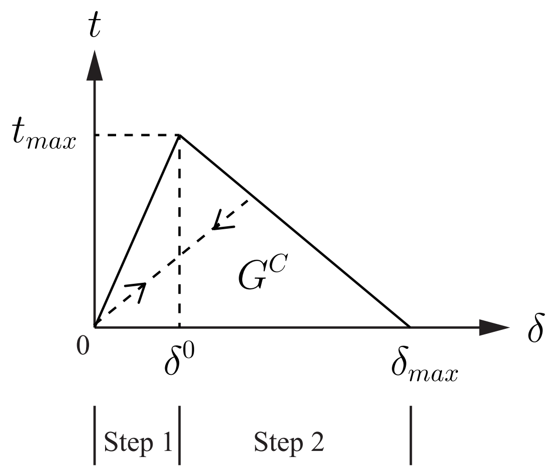


Figure 5: Traction-separation law for the used cohesive elements.

In Fig. 5, $G^C$ is the fracture energy of interface debonding with mixed modes, in which normal and shear separations occur at the same time. It is expressed using the Benzeggagh-Kenane fracture criterion, and written as in Eq.(16).

$$G^C = G_n^C + (G_s^C - G_n^C)(\frac{G_s^C + G_t^C}{G_s^C + G_n^C})^\eta \tag{16}$$

where, $G_n^C$, $G_s^C$ and $G_t^C$ are critical values of fracture energy required to cause failure in the normal, the first and the second shear directions, and $\eta$ denotes a cohesive property parameter. This CZM approach has been also integrated and implemented in a VUMAT user subroutine in Abaqus/Explicit [32] to predict the damage behavior of the adhesive bondline.

## 4. Results and discussion

In this section, firstly, the validation procedure of the used numerical model is explained using the experimental and numerical results. Then, the influence of different patch design parameters on repair performance is investigated based on this numerical simulation. Finally, the optimal patch design that includes patch shape and size, is determined with the help of the proposed predictive model.

### *4.1. Validation of numerical models*

For the purpose of validation, numerical models have been built based on the drop-weight tests presented in Section 2.2. Accordingly, numerical drop-weight tests have been performed for repaired specimens with circular and hexagonal patches. The predicted and experimental time history curves of the impact force and energy are shown in Figs. 6 and 7, respectively.

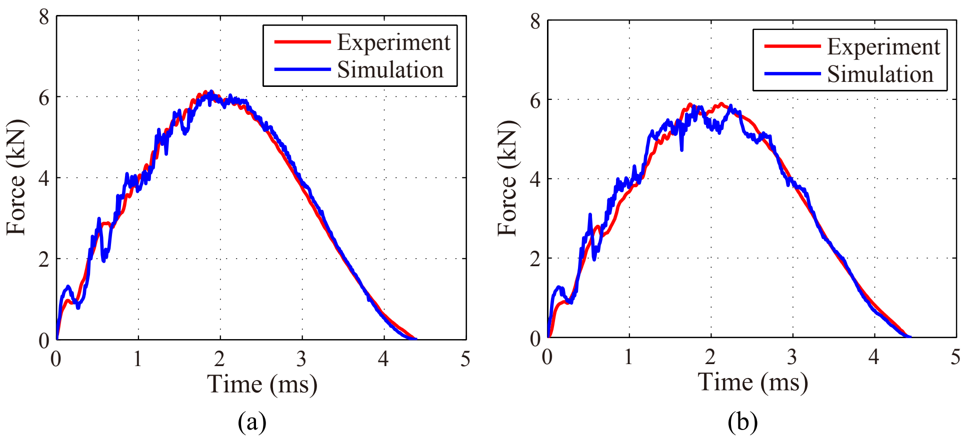


Figure 6: Experimental and predicted impact force history curves of repaired specimens with (a) circular and (b) hexagonal patches as a function of time.

From Fig. 6, it can be found that, in the case of specimen repaired with circular patch, the measured force peak is 6124.2 N while the predicted one is 6135.4 N. Only a slight discrepancy of 0.18% exists in this comparison. In the case of hexagonal patch, these values are 5891.9 N and 5847.7 N respectively and it provides the corresponding difference of less than 0.76%. In addition,

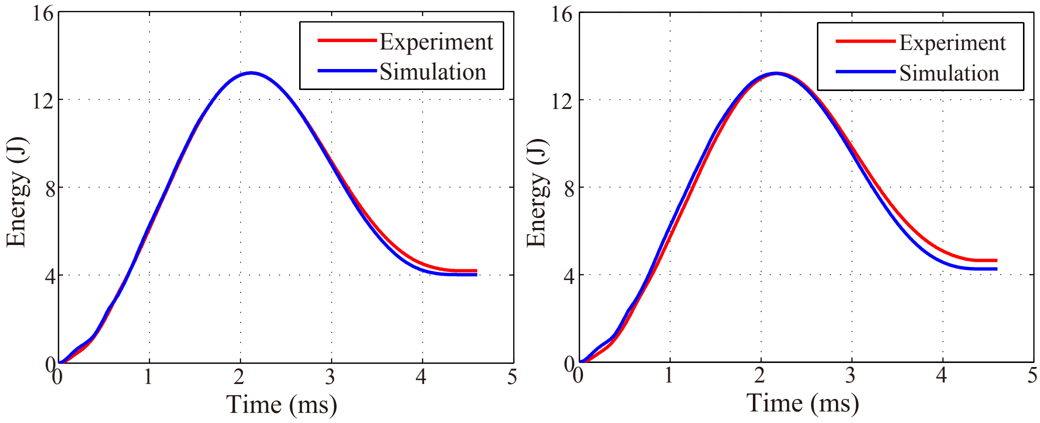


(a) (b)

Figure 7: Experimental and predicted impact energy history curves of repaired specimens with (a) circular and (b) hexagonal patches as a function of time.

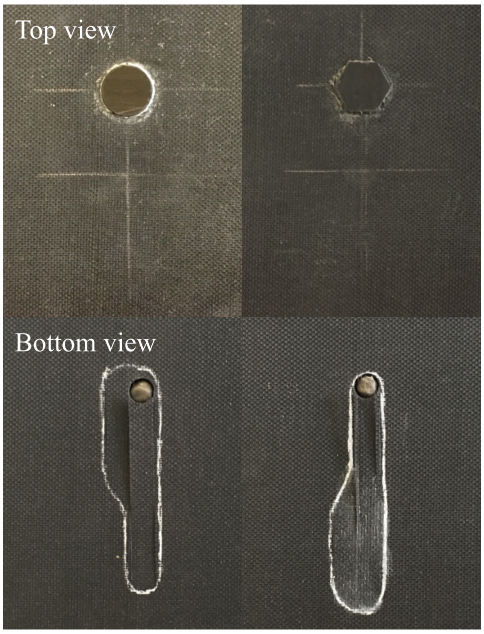


(a) (b)

Figure 8: Top and bottom views of the specimens repaired with (a) circular and (b) hexagonal patches, from the experimental tests. Delamination surface has been denoted by with the line on each specimen's back side.

energy history curves show that, there exists almost no difference in the maximum impact energy and its corresponding time (Fig. 7).

To further confirm the robustness of the used damage prediction criteria, another comparison of the delamination surface area has been implemented. Fig. 8 shows the top and bottom views of specimens repaired with circular and hexagonal patches after experimental tests. The bottom view of the specimen indicates the damage level more directly and clearly so that white line has drawn on each specimen's back side to take measure of the delamination surface area. Accordingly, the

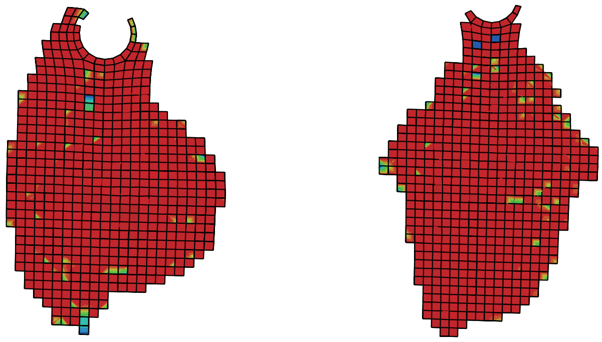

(a) (b)

Figure 9: The delamination surface of specimens repaired with (a) circular and (b) hexagonal patches, from numerical simulation.

delamination surface of each specimen after numerical impact simulation is shown in Fig. 9. Here, this delamination surface consists of all cohesive elements between various layers deleted during the impact process. By counting the delamination surface area of each specimen: in the case of experimental tests, the surface areas are approximately 558 mm$^2$ and 572 mm$^2$ for circular and hexagonal patches respectively. In the numerical case, these values are 579 mm$^2$ and 583 mm$^2$ for the circular and hexagonal repair patches, respectively. The difference of these two specimens is less than 3.80% and 1.90%, respectively. Hence, it is concluded that, a good agreement is reached for these two specimens repaired with circular and hexagonal patches.

### *4.2. Influence of patch design parameters on the repair performance*

Robustness of the proposed numerical modeling approach is shown in the previous section. Therefore, this numerical model is used to study the influence of different patch design parameters, which includes patch shape and size, on the repair performance.

#### *4.2.1. Influence of patch shape*

The influence of patch shape on the repair performance is studied by performing numerical simulation of different specimens. The damaged laminate plates are repaired with five types of patch shapes: circle, square, rhombus (slanted square), hexagon and octagon, as shown in Fig. 10. In order to eliminate the effect of other origins on the repair performance, the surface area of these patches is chosen as equal to 113.1 mm$^2$, in which case the radius of circle patch equals to $2r$ (2 times of the hole radius on parent laminate). Same element size is also used to mesh all these patches.

Impact force curves of specimens repaired with different patches are depicted from the numerical simulations as shown in Fig. 11. It can be found that, for each specimen, the oscillation tendency of impact force appears in the same way during the whole impact process. It indicates that, the onset of damage in each specimen occurs almost at the same location of the history curves. However, by comparing the oscillation magnitude of impact force in these cases, several observations can be obtained: the minimum impact force variation takes place in the case of specimen repaired with circular patch, while the maximum force oscillation appears in the specimen repaired with rhombus patch. It means that, the repaired structure with the circular patch absorbs

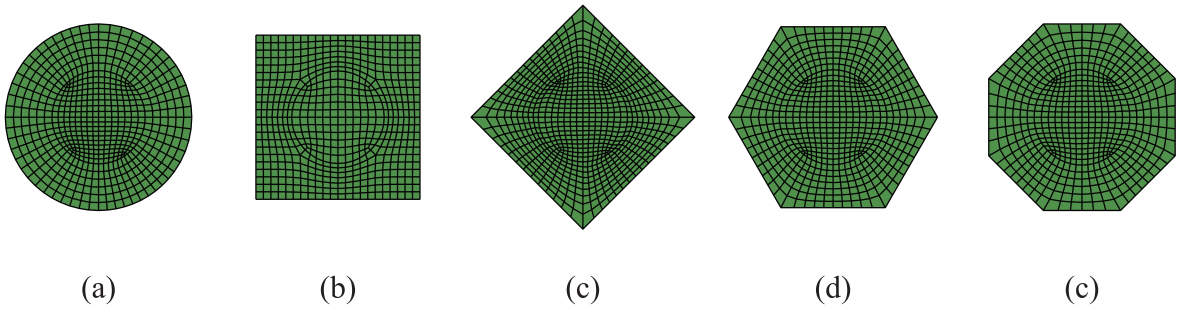


Figure 10: FE models of five patches with different shapes: (a) circle, (b) square, (c) rhombus (slanted square), (d) hexagon and (c) octagon.

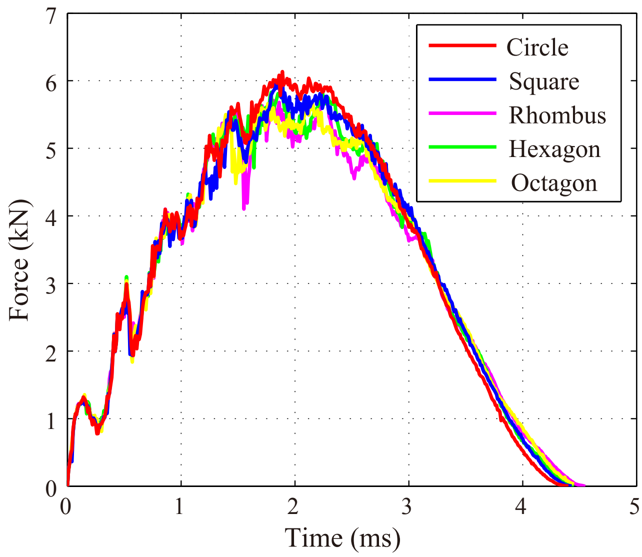


Figure 11: Predicted impact force curves of specimens repaired with different patch shapes.

less impact energy than others, while the one with the rhombus patch absorbs the highest energy. In other word, the repair performance of the circular patch is better than other patch shapes. This ...

Table 2: Numerical results of specimens repaired with different patch shapes.

| Patch shape | Force peak (N) | Absorbed energy (J) | Delamination area ($mm^2$) |
|---|---|---|---|
| Circle | 6135.4 | 4.02 | 579 |
| Square | 6019.9 | 4.39 | 592 |
| Rhombus | 5738.2 | 4.95 | 682 |
| Hexagon | 5847.7 | 4.26 | 583 |
| Octagon | 5675.6 | 4.75 | 643 |

Additionally, another comparison of predicted impact energy curves of different repaired spec-

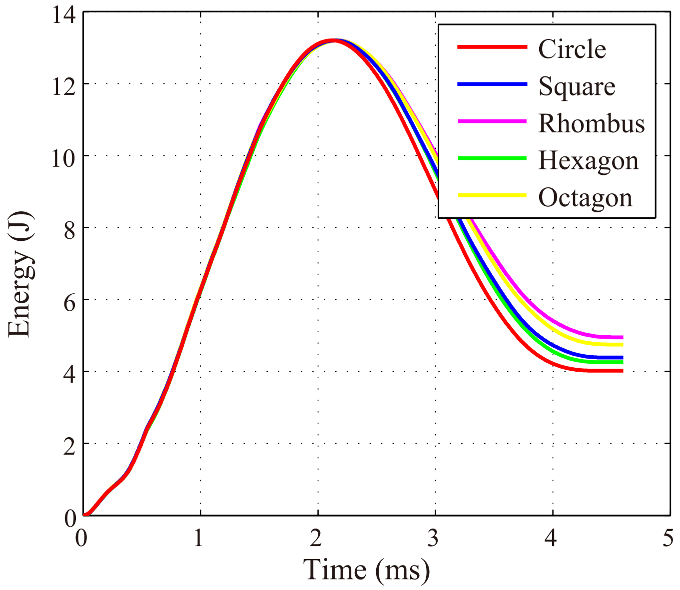


Figure 12: Predicted impact energy curves of specimens repaired with different patch shapes.

imens has been performed based on the simulation results, as shown in Fig. 12. The specimen repaired with circle patch (red solid line), absorbs the minimum impact energy whose value is 4.02 J. And, the maximum impact energy absorbed by repaired specimen is the case of rhombus patch (pink solid line). Detailed information of force peak, energy absorbed and delamination surface area in each case is listed in Table 2. It also supports that the repair performance of the circular patch is relatively better. Moreover, by comparing the delamination area, it can be found that, the circular patch improves mechanical performance of damaged laminate around 2.2%, 15.1%, 0.7% and 10% better than square, rhombus, hexagon and octagon ones, respectively. The main reason is that, the circular patch distributes the stress evenly around the whole area, that provides the better performance compared to other patch shapes. Moreover, since the other patches have sharp corners, it may facilitate a stress concentration and the damage compared to that of the circular patch. The circular patch can also lead to a minor stress concentration on the repaired specimen than others. Therefore, in the term of patch shape, circle patch is the optimal choice to repair the damaged laminate with hole.

#### *4.2.2. Influence of patch size*

Since circle is proved as the optimal shape to improve the mechanical behavior of damaged laminate with hole, the influence of patch size is studied using circle patch. Consequently, numerical drop-weight tests have been performed on a set of 7 circle patches with radius ranging from 1.5r to 3.5r (r: hole radius).

Accordingly, history curves of impact force and energy are depicted in Figs. 13 and 14, respectively. As shown in Fig. 13, the maximum fluctuation of impact force appears in the case of patch with radius 1.5r. And, other cases have the same oscillation tendency, in which peak force occurs at 1.8 ms. Furthermore, by comparing curves in Fig. 14, the patch size of 1.5r makes the repaired laminate absorb more impact energy than others. In the remaining cases, the energy curve

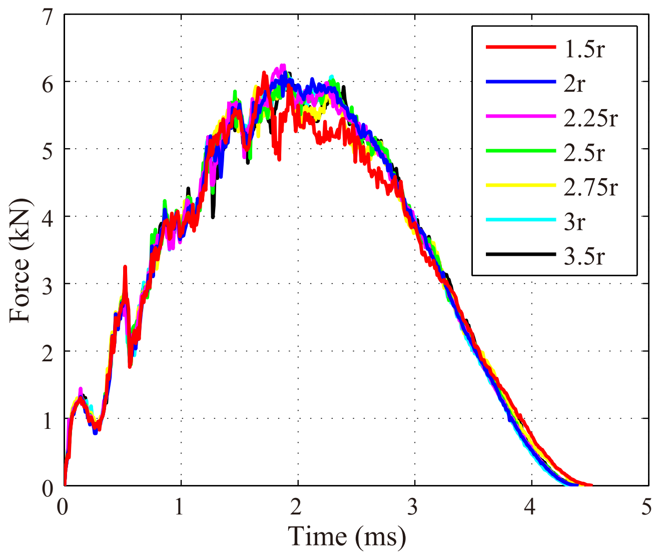


Figure 13: Predicted impact force curves of specimens repaired with different patch sizes.

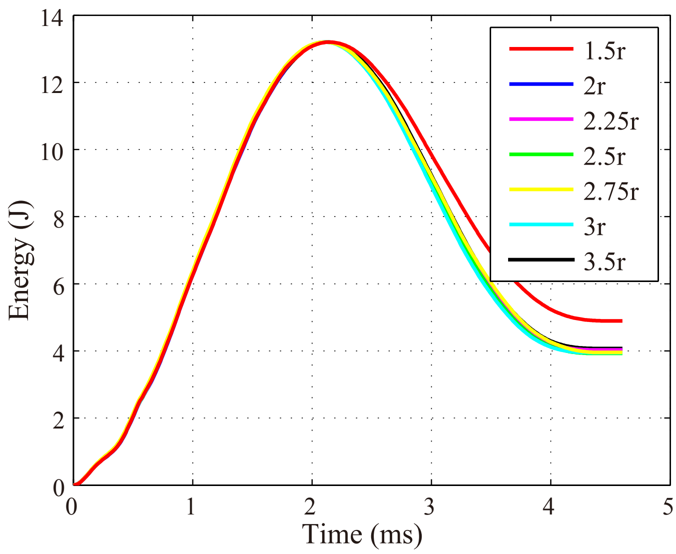


Figure 14: Predicted impact energy curves of specimens repaired with different patch sizes.

is too close to each other. However, based on the absorbed energy and delamination area listed in Table 3, the patch with radius of 2.5r leads to a better repair performance.

The relationship between patch radius with absorbed energy and delamination area is illustrated in Fig. 15. From this figure, it clearly indicates that, as the patch size increasing, both of the absorbed energy and delamination area curves decrease. When the radius patch comes to 2.5r, the corresponding damage level after impact gets to the minimum one. It also confirms that, the specimen repaired with 2.5r patch has better impact resistance behavior. Afterwards, when the radius

Table 3: Numerical results of specimens repaired with different patch sizes.

| Patch size | Force peak (N) | Absorbed energy (J) | Delamination area ($mm^2$) |
|---|---|---|---|
| 1.5r | 6133.4 | 4.89 | 610 |
| 2r | 6035.4 | 4.02 | 579 |
| 2.25r | 6290.9 | 4.03 | 573 |
| 2.5r | 6147.7 | 3.93 | 570 |
| 2.75r | 6119.1 | 3.96 | 587 |
| 3r | 6107.8 | 3.95 | 592 |
| 3.5r | 6119.2 | 4.07 | 576 |

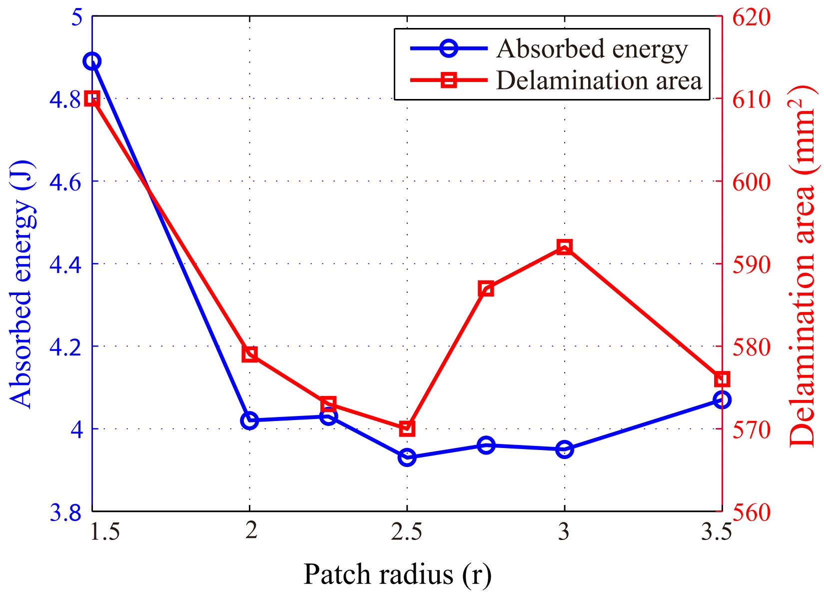


Figure 15: Predicted impact energy curves of specimens repaired with different patch sizes.

exceeds this size, the absorbed energy of the repaired specimens fluctuates around the converged value. While, the delamination area curve initially increases from 570 $mm^2$ to 592 $mm^2$, and then it stabilizes at around 580 $mm^2$.

The difference of these two curves is probably caused by the different penetration depth of impactor into the repaired specimens. That is, the deeper the impactor penetrates into specimen, the more energy is absorbed, and vice versa. Furthermore, the repair performance demonstrates in not only in-plane direction, but also out-of-plane direction. When the patch radius reaches the converged size, the anti-impact behavior of out-of-plane direction is mainly improved by the big patch. Then, the impactor cannot penetrates as deep as other repaired specimens, which leads to a larger delamination surface of the specimen. Therefore, as patch radius increasing, the value of absorbed energy is at the same level, a significant fluctuation appears in the delamination area curve. The validation of this assumption requires further experimental and numerical investigations. For now, the corresponding work has a limitation to investigate the penetration depth due to the difficulty of making experimental measurements using the current setup. Based on the numerical results, we can conclude that, the absorbed energy is a suitable physical variable to evaluate the repair performance.

### *4.3. Determination of the optimal patch design*

As presented in previous section, influence of different patch design parameters on the repair performance has been discussed, which include patch shape and size. Specimen repaired with circle patch demonstrates better impact resistance behavior. Therefore, the optimal patch design should be with a circle geometry. An approximate converged patch size is also obtained as 2.5r. To complement the optimal patch design, a tentative to set up an empirical relationship between patch radius and absorbed energy is described in this section. The proposed relationship is based on simulation results.

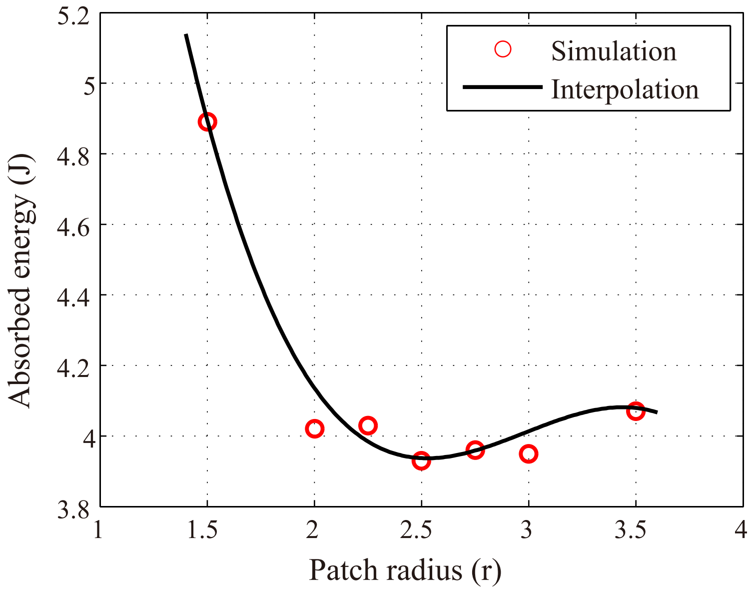


Figure 16: Interpolation relationship between patch radius and the absorbed energy.

Based on the obtained results, a 3rd order polynomial interpolation is constructed to indicate the relationship between patch radius $R$ and the absorbed energy $E_{\text{abs}}$. The form of aforementioned polynomial interpolation is given by the following equation:

$$E_{\text{abs}} = -0.3805R^3 + 3.404R^2 - 9.913R + 13.39 \tag{17}$$

Fig. 16 shows the absorbed energy as a function of patch radius, and the predicted points are depicted by red circles. It reveals that, the optimal patch size is located around 2.53r. Here, we use the patch with radius 2.5r as the optimal one. Therefore, in this study, the optimal patch design is circle geometry with radius of 2.5r.

Additionally, a numerical drop-weight test is performed on the unrepaired specimen to evaluate the repair performance of the optimal patch design. Fig. 17 illustrates the predicted impact energy curves of these two cases (optimal patch design and unrepaired specimen). At the ends of these

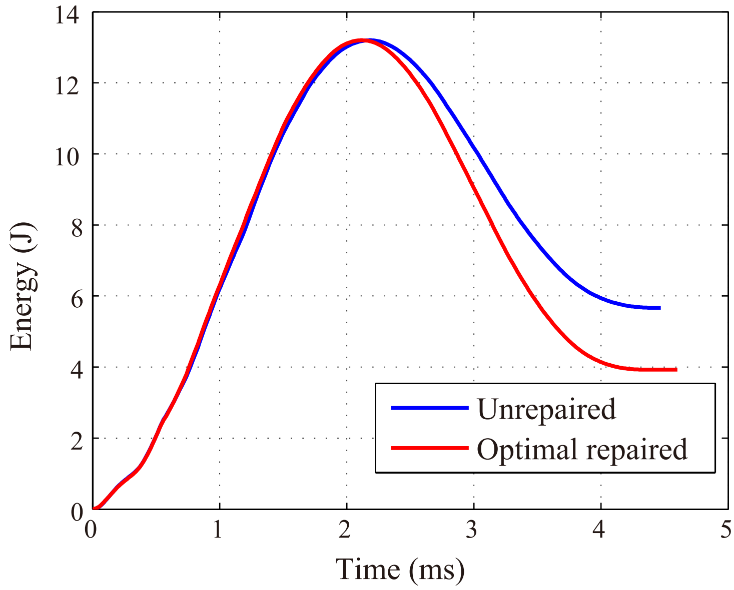


Figure 17: Predicted impact energy curves of unrepaired and optimal repaired specimens.

two curves, the values of absorbed energy are 5.67 J and 3.93 J for the unrepaired and optimal repaired specimens, respectively. Hence, the optimal patch design has the capacity to improve the impact resistance behavior of damaged laminate by 30.7%. The external patch-repaired operation, in which proper parameters are used, can effectively restore the mechanical properties of damaged composite structures. Besides, the repair performance is affected by many other factors, e.g., the used adhesive, surface preparation of parent laminate, patch thickness. Extension of the work on this subject will necessitate to take into account the influence of these factors.

## 5. Conclusions and perspectives

In this study, the low-velocity impact behavior of patch-repaired CFRP laminates has been investigated using numerical and experimental approaches. Patch-repaired specimens were manufactured with the parent laminates in which a hole is considered as the existing damage. Experimental and numerical low-velocity impact tests have been successfully implemented to study the influence of various patch design parameters, such as shape and size on the repair performance. Based on interpolation method, optimal patch design was determined to get a relatively superior repair performance.

Additionally, results of impact force and energy from numerical simulation corroborate the experimental observation. Especially, the predicted delamination surface area of specimens after impact closely resembles with the experimental measurement. Both of these results indicate the accuracy and reliability of the numerical simulation method. Furthermore, due to the limitation of our present experimental conditions, only the influence of patch shape and size was discussed using proposed numerical approach. In the parametric study of patch shapes of: circle, square, rhombus, hexagon and octagon patches with the same area, were utilized to repair the damaged laminates. From the comparison of absorbed energy and delamination area in each case, the circle patch leads to a better repair performance. It is also found that, the optimal radius for circle patch is 2.5 times of the damage hole. Moreover, it is observed that, as patch radius increasing, the energy absorbed by each specimens stay the same level, while the corresponding delamination area is significantly different. This is possibly caused by the different penetration depth within each specimen. However, it needs further experimental and numerical investigations. Compared with unrepaired specimen, the optimal patch design significantly enhances the anti-impact behavior of damaged laminates.

This primary study also provides the foundation for relevant parametric study with the consideration of advanced structural optimization methods, such as shape optimization [36] and topology optimization [37–39] techniques, to search the optimum patch design. During the extension in topology optimization problem, the key difficulties are: (1) the construction of the interface between the numerical model and the optimization algorithm, (2) the choice of the proper optimization algorithm. These challenges will be untangled in our future work.

Overall, this study provides a novel orientation to investigate the low-velocity impact behavior of patch-repaired CFRP laminates experimentally and numerically. It could be implemented and further extended for various repair techniques developed for composite materials.

## Acknowledgements

Authors acknowledge the sponsorship and support from Natural Science Foundation of China (NSFC, U1333201), and the China Postdoctoral Science Foundation Funded Project (2016M60225 6). This study is also supported by the Fundamental Research Funds of Zhengzhou University (F0001261), and Excellent Talented Teacher Project (1521321036).

## References

[1] R. Jones, W. Chiu, R. Smith, Airworthiness of composite repairs: failure mechanisms, Engineering Failure Analysis 2 (2) (1995) 117–128.

[2] Z. P. Marioli-Riga, X. Dionissios, Repairability and cost analysis criteria for typical composite patch repairs, Facta universitatis-series: Mechanics, Automatic Control and Robotics 3 (14) (2003) 951–962.

[3] M. Charalambides, R. Hardouin, A. Kinloch, F. Matthews, Adhesively-bonded repairs to fibre-composite materials i. experimental, Composites Part A: Applied Science and Manufacturing 29 (11) (1998) 1371–1381.

[4] M. Charalambides, A. Kinloch, F. Matthews, Adhesively-bonded repairs to fibre-composite materials ii. finite element modelling, Composites Part A: Applied Science and Manufacturing 29 (11) (1998) 1383–1396.

[5] C. Soutis, F. Hu, Design and performance of bonded patch repairs of composite structures, Proceedings of the Institution of Mechanical Engineers, Part G: Journal of Aerospace Engineering 211 (4) (1997) 263–271.

[6] X.-J. Gong, P. Cheng, S. Aivazzadeh, X. Xiao, Design and optimization of bonded patch repairs of laminated composite structures, Composite Structures 123 (2015) 292–300.

[7] M. Ramji, R. Srilakshmi, M. B. Prakash, Towards optimization of patch shape on the performance of bonded composite repair using fem, Composites Part B: Engineering 45 (1) (2013) 710–720.

[8] M. Kashfuddoja, M. Ramji, Design of optimum patch shape and size for bonded repair on damaged carbon fibre reinforced polymer panels, Materials & Design (1980-2015) 54 (2014) 174–183.

[9] B. Whittingham, A. Baker, A. Harman, D. Bitton, Micrographic studies on adhesively bonded scarf repairs to thick composite aircraft structure, Composites Part A: Applied Science and Manufacturing 40 (9) (2009) 1419–1432.

[10] C. H. Wang, A. J. Gunnion, On the design methodology of scarf repairs to composite laminates, Composites Science and Technology 68 (1) (2008) 35–46.

[11] C. H. Wang, A. J. Gunnion, Optimum shapes of scarf repairs, Composites Part A: Applied Science and Manufacturing 40 (9) (2009) 1407–1418.
[12] T. Breitzman, E. Iarve, B. Cook, G. Schoeppner, R. Lipton, Optimization of a composite scarf repair patch under tensile loading, composites Part A: Applied science and manufacturing 40 (12) (2009) 1921–1930.
[13] F. Hu, C. Soutis, Strength prediction of patch-repaired cfrp laminates loaded in compression, Composites Science and Technology 60 (7) (2000) 1103–1114.
[14] X. Liu, G. Wang, Progressive failure analysis of bonded composite repairs, Composite Structures 81 (3) (2007) 331–340.
[15] M. Caminero, M. Lopez-Pedrosa, C. Pinna, C. Soutis, Damage monitoring and analysis of composite laminates with an open hole and adhesively bonded repairs using digital image correlation, Composites Part B: Engineering 53 (2013) 76–91.
[16] P. Cheng, X.-J. Gong, D. Hearn, S. Aivazzadeh, Tensile behaviour of patch-repaired cfrp laminates, Composite structures 93 (2) (2011) 582–589.
[17] P. Cheng, X.-J. Gong, S. Aivazzadeh, X. Xiao, Experimental observation of tensile behavior of patch repaired composites, Polymer Testing 34 (2014) 146–154.
[18] C. Soutis, D. Duan, P. Goutas, Compressive behaviour of cfrp laminates repaired with adhesively bonded external patches, Composite structures 45 (4) (1999) 289–301.
[19] Y. Xu, H. Lu, T. Gao, W. Zhang, Predicting the low-velocity impact behavior of polycarbonate: Influence of thermal history during injection molding, International Journal of Impact Engineering 86 (2015) 265–273.
[20] M. Richardson, M. Wisheart, Review of low-velocity impact properties of composite materials, Composites Part A: Applied Science and Manufacturing 27 (12) (1996) 1123–1131.
[21] C. Santiuste, S. Sánchez-Sáez, E. Barbero, A comparison of progressive-failure criteria in the prediction of the dynamic bending failure of composite laminated beams, Composite Structures 92 (10) (2010) 2406–2414.
[22] J. J. Andrew, V. Arumugam, K. Saravanakumar, H. N. Dhakal, C. Santulli, Compression after impact strength of repaired gfrp composite laminates under repeated impact loading, Composite Structures 133 (2015) 911–920.
[23] S. Coelho, P. Reis, J. Ferreira, A. Pereira, Effects of external patch configuration on repaired composite laminates subjected to multi-impacts, Composite Structures 168 (2017) 259–265.
[24] H. Singh, K. K. Namala, P. Mahajan, A damage evolution study of e-glass/epoxy composite under low velocity impact, Composites Part B: Engineering 76 (2015) 235–248.
[25] Z. HASHI, Failure criteria for unidirectional fiber composite, Journal of Applied Mechanics 47 (1980) 3292334.
[26] D.-H. Kim, K.-H. Jung, I.-G. Lee, H.-J. Kim, H.-S. Kim, Three-dimensional progressive failure modeling of glass fiber reinforced thermoplastic composites for impact simulation, Composite Structures 176 (2017) 757–767.
[27] S. Long, X. Yao, X. Zhang, Delamination prediction in composite laminates under low-velocity impact, Composite Structures 132 (2015) 290–298.
[28] R. Campilho, M. De Moura, J. Domingues, Stress and failure analyses of scarf repaired cfrp laminates using a cohesive damage model, Journal of Adhesion Science and Technology 21 (9) (2007) 855–870.
[29] M. De Moura, J. Gonçalves, J. Chousal, R. Campilho, Cohesive and continuum mixed-mode damage models applied to the simulation of the mechanical behaviour of bonded joints, International Journal of adhesion and Adhesives 28 (8) (2008) 419–426.
[30] F. Benyahia, A. Albedah, B. B. Bouiadjra, Analysis of the adhesive damage for different patch shapes in bonded composite repair of aircraft structures, Materials & Design (1980-2015) 54 (2014) 18–24.
[31] ASTM D7136/D7136M-07 standard test method for measuring the damage resistance of a fiber-reinforced polymer matrix composite to a drop-weight impact event, 2003.
[32] Hibbitt, Karlsson, Sorensen, ABAQUS/Explicit: user's manual, Vol. 1, Hibbitt, Karlsson and Sorenson Incorporated, 2001.
[33] J.-F. Chen, E. V. Morozov, K. Shankar, Simulating progressive failure of composite laminates including in-ply and delamination damage effects, Composites Part A: Applied Science and Manufacturing 61 (2014) 185–200.
[34] L. Jia, L. Yu, K. Zhang, M. Li, Y. Jia, B. Blackman, J. Dear, Combined modelling and experimental studies of failure in thick laminates under out-of-plane shear, Composites Part B: Engineering 105 (2016) 8–22.
[35] F. Aymerich, F. Dore, P. Priolo, Prediction of impact-induced delamination in cross-ply composite laminates

using cohesive interface elements, Composites science and technology 68 (12) (2008) 2383–2390.

[36] S. Cai, W. Zhang, J. Zhu, T. Gao, Stress constrained shape and topology optimization with fixed mesh: a b-spline finite cell method combined with level set function, Computer Methods in Applied Mechanics and Engineering 278 (2014) 361–387.

[37] Y. Hou, T. Sapanathan, A. Dumon, P. Culière, M. Rachik, A novel artificial dual-phase microstructure generator based on topology optimization, Computational Materials Science 123 (2016) 188–200.

[38] L. Xia, P. Breitkopf, Recent advances on topology optimization of multiscale nonlinear structures, Archives of Computational Methods in Engineering 24 (2) (2017) 227–249.

[39] L. Xia, D. Da, J. Yvonnet, Topology optimization for maximizing the fracture resistance of quasi-brittle composites, Computer Methods in Applied Mechanics and Engineering 332 (2018) 234–254.